Available online at www.sciencedirect.com
ScienceDirect
Trans. Nonferrous Met. Soc. China 30(2020) 2737−2748
Transactions of Nonferrous Metals Society of China
www.tnmsc.cn

Microstructure evolution and hot deformation behavior of Cu–3Ti–0.1Zr alloy with ultra-high strength

Xu WANG[1], Zhou LI[1,2], Zhu XIAO[1,3], Wen-ting QIU[1]

1. School of Materials Science and Engineering, Central South University, Changsha 410083, China;
2. State Key Laboratory of Powder Metallurgy, Central South University, Changsha 410083, China;
3. Key Laboratory of Non-ferrous Metal Materials Science and Engineering, Ministry of Education, Changsha 410083, China

Received 7 February 2020; accepted 28 June 2020

Abstract: The hot compression deformation behavior of Cu−3Ti−0.1Zr alloy with the ultra-high strength and good electrical conductivity was investigated on a Gleeble−3500 thermal-mechanical simulator at temperatures from 700 to 850 °C with the strain rates between 0.001 and 1 s^{-1}. The results show that work hardening, dynamic recovery and dynamic recrystallization occur in the alloy during hot deformation. The hot compression constitutive equation at a true strain of 0.8 is constructed and the apparent activation energy of hot compression deformation Q is about 319.56 kJ/mol. The theoretic flow stress calculated by the constructed constitutive equation is consistent with the experimental result, and the hot processing maps are established based on the dynamic material model. The optimal hot deformation temperature range is between 775 and 850 °C and the strain rate range is between 0.001 and 0.01 s^{-1}.

Key words: Cu−3Ti−0.1Zr alloy; hot deformation; constitutive equation; recrystallization; hot processing map

1 Introduction

Copper based elastic alloys with high strength and good electrical conductivity have been widely used in electronic and electrical industries [1−4]. The frequently-used copper−beryllium alloys have a ultra-high strength higher than 1000 MPa and a relative high electrical conductivity of 22% IACS [5]. However, the element beryllium in the alloy is toxic during the manufacturing process and lots of elastic alloys without beryllium element, such as Cu−Ti alloys [6], Cu−Ni−Si alloys [1,7] and Cu–Ni–Sn alloys [4,8] have been developed to substitute for Cu−Be alloy. In recent years, the Cu−Ti alloys have been paid a great attention owing to their excellent comprehensive properties. As typical age strengthening alloys, Cu−Ti alloys have high elasticity, heat resistance, fatigue resistance as well as the relative low bending radius ratio (R/t) among the ultra-high strength copper alloys. Cu−Ti alloys are environmentally friendly and low-cost compared with the traditional high strength Cu−Be alloy, and they also possess a high bending tolerance performance compared with Cu−Ni−Si alloy and Cu−Ni−Sn alloy. The Cu−Ti alloys including YCuT−F, HPTC and NKT322 (which has a tensile strength of 1200 MPa and electrical conductivity of 13% IACS) have been developed for potential application on connectors and springs in electronic field.

However, the hot workability of the Cu−Ti

Foundation item: Project (2016YFB0301300) supported by the National Key Research and Development Program of China; Project (U1637210) supported by the National Natural Science Foundation of China; Project (2019B10088) supported by the Technology Research Program of Ningbo, China; Project supported by State Key Laboratory of Powder Metallurgy, Central South University, China

Corresponding author: Zhu XIAO; Tel: +86-13974910804; E-mail: xiaozhumse@163.com

DOI: 10.1016/S1003-6326(20)65416-4

alloys is poor [9] and the hot rolling cracks easily occur during hot deformation. Constitutive equations and hot processing maps based on dynamic material model (DMM) are usually applied to predicting the hot deformation processes of alloys. This method is widely used for various alloys, such as Al [10], Ti [11], Mg [12], Cu [13,14] alloys and different kinds of steel [15]. The hot deformation behavior of these alloys, including work hardening, dynamic recovery (DRV) and dynamic recrystallization (DRX), have been studied. It has been reported that the precipitates also have a great effect on the hot deformation behavior of the alloys [14,16,17]. Generally speaking, the precipitates with the size of 0.5−2 μm could promote the nucleation of DRX, while those with the size smaller than 0.5 μm would pin the dislocation and hinder the migration of grain boundary, which inhibits the process of DRX [16]. Up to now, even though there have been some researches on constitutive equations and hot processing maps of Cu−Ti alloys [9,14,18,19], little work has been done on the hot deformation behavior of Cu−3Ti−0.1Zr alloy. It is necessary to study the evolution of deformation microstructure and dynamic recrystallization (DRX) of the alloy during hot working systematically.

In this work, hot deformation behavior of Cu−3Ti−0.1Zr alloy with ultra-high strength was investigated by hot compression deformation testing. The hot deformation temperature range in the test was from 700 to 850 °C with the strain rate from 0.001 to 1 s^{-1}. Microstructure evolution was studied using optical microscope (OM) and transmission electron microscope (TEM) in order to analyze the influence of temperature and strain rate on hot deformation behavior of the alloy. Constitutive equation and hot processing maps were established according to the flow stress curves of the alloy during deformation. The results in this work can guide the hot working of Cu−3Ti−0.1Zr alloy and provide the reference data for the Cu−Ti-based alloys.

2 Experimental

The ingot of Cu−3Ti−0.1Zr (wt.%) alloy was melted in a medium frequency induction furnace, with the raw materials of pure copper (purity of 99.95%), Cu−25%Ti master alloy and Cu−20%Zr master alloy. The ingot was homogenized at 920 °C for 2 h. Cylindrical specimens with the diameter of 8 mm and the height of 12 mm were prepared using spark-erosion wire cutting.

Hot compression deformation simulation experiment was carried out on a Gleeble−3500 thermal simulator. The deformation temperatures were 700, 750, 800 and 850 °C, and the strain rates were 1, 0.1, 0.01 and 0.001 s^{-1} with a total true strain of 0.9. Before compression, the specimens were heated to the testing temperatures at a heat rate of 5 °C/s and then held at the given temperature for 3 min. After compression, the specimens were quenched into the water quickly. Figure 1 shows the schematic illustration of the whole test.

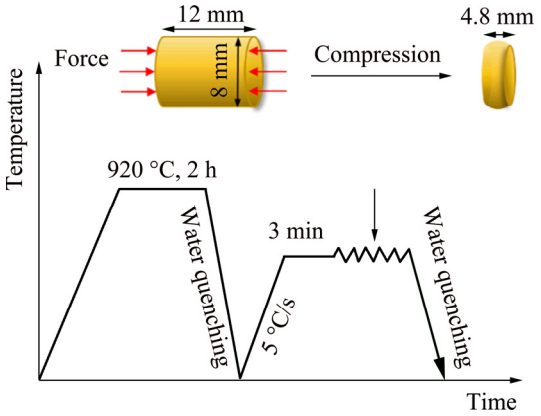

Fig. 1 Schematic illustration of specimen and experiment process

The OM specimens were etched in a solution of $FeCl_3$ (5 g), HCl (25 mL) and deionized water (75 mL) after mechanical polishing. The OM images were taken by a Leica DM6000M microscope. TEM samples were electro-polished between −30 and −20 °C with a Struers Tenupol−5 electrolytic instrument. The content of electro-polishing solution was 30% HNO_3 and 70% CH_3OH. The observation was carried out using Tecnai $G^2$20 transmission electron microscope.

3 Results and discussion

3.1 True stress–true strain curves

The true stress–true strain curves of Cu−3Ti−0.1Zr alloy deformed at different temperatures and different strain rates are shown in Fig. 2. Deformation temperatures and strain rates have significant influence on the flow stress. The flow stress increases with the increase of strain rate

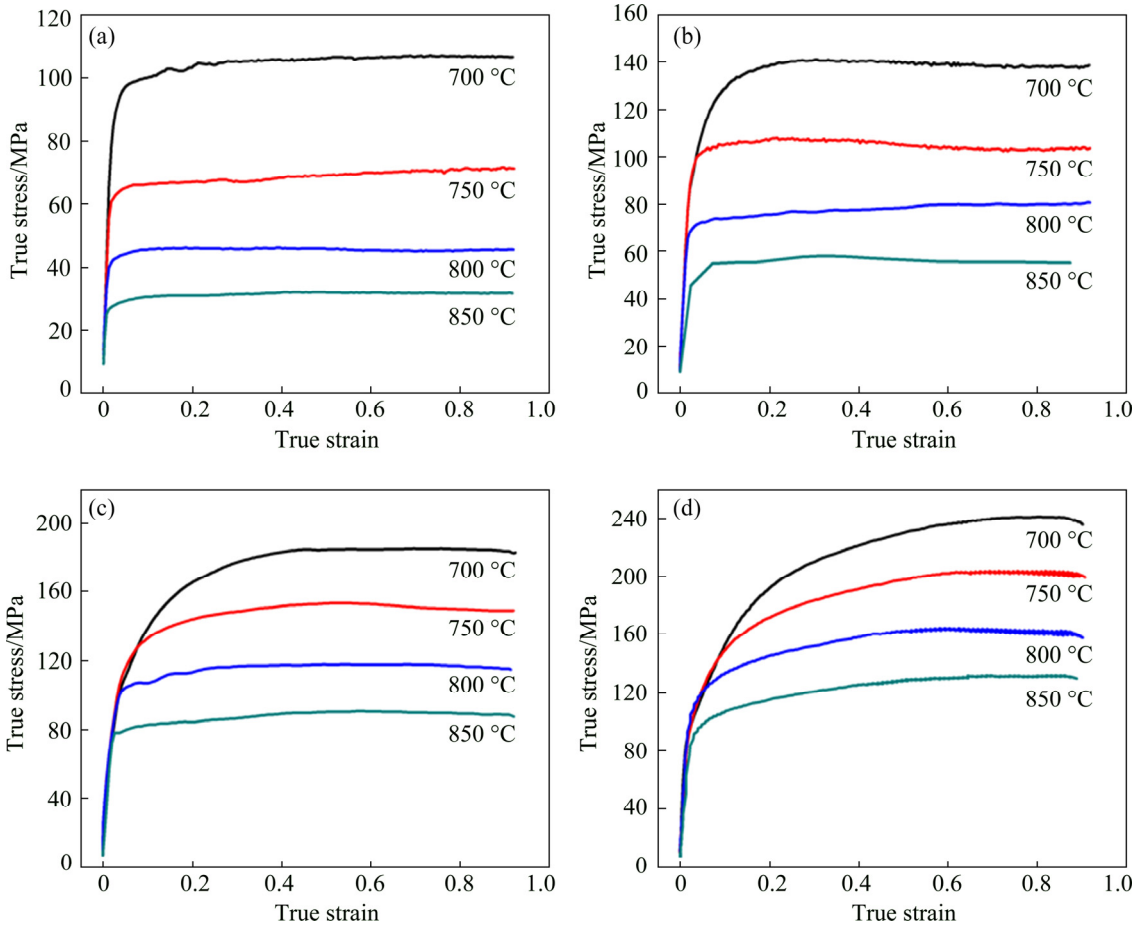

Fig. 2 True stress–true strain curves of Cu−3Ti−0.1Zr alloy deformed at different temperatures and strain rates: (a) 0.001 s^{-1}; (b) 0.01 s^{-1}; (c) 0. 1 s^{-1}; (d) 1 s^{-1}

and decreases with the increase of deformation temperatures. For the specimens deformed at the strain rates below 1 s^{-1} (Figs. 2(a−c)), the whole deformation process can be divided into three parts: (1) at the early stage of deformation, flow stress increases rapidly to a maximum value because of work hardening; (2) at the second stage, flow stress increases slowly owing to dynamic recovery (DRV) and dynamic recrystallization (DRX); (3) at the third stage, flow stress keeps stable, which is caused by balance between work hardening and softening.

However, the true stress–true strain curves for specimens deformed at the strain rates of 1 s^{-1} (Fig. 2(d)) are different from those shown in Figs. 2(a−c). Typical continuous strain hardening can be easily found in Fig. 2(d). Dynamic recovery is the main softening mechanism at high deformation strain rate, especially when the deformation temperature is low. At the same time, the work hardening is dominated compared with the softening of DRV, leading to the slight increase of flow stress.

The oscillation of flow stress is obvious in all specimens (especially clear in Fig. 2(d)), indicating a discontinuous yielding phenomenon. This is attributed to the stress concentration and relaxation that happen at grain boundaries or inside the grains, resulting in the fluctuation of the flow stress [20].

3.2 Microstructure evolution

The microstructures of Cu−3Ti−0.1Zr alloy deformed at different temperatures and strain rates are shown in Fig. 3. Elongated grains perpendicular to the compression direction are found in specimen deformed at 700 °C and 1 s^{-1} (Fig. 3(a)) and the crack along grain boundary appears. The same structure is found in specimen deformed at 750 °C and 1 s^{-1} (Fig. 3(b)). A cavity forms at the junction of grain boundaries under this deformation condition due to the decrease of grain boundary

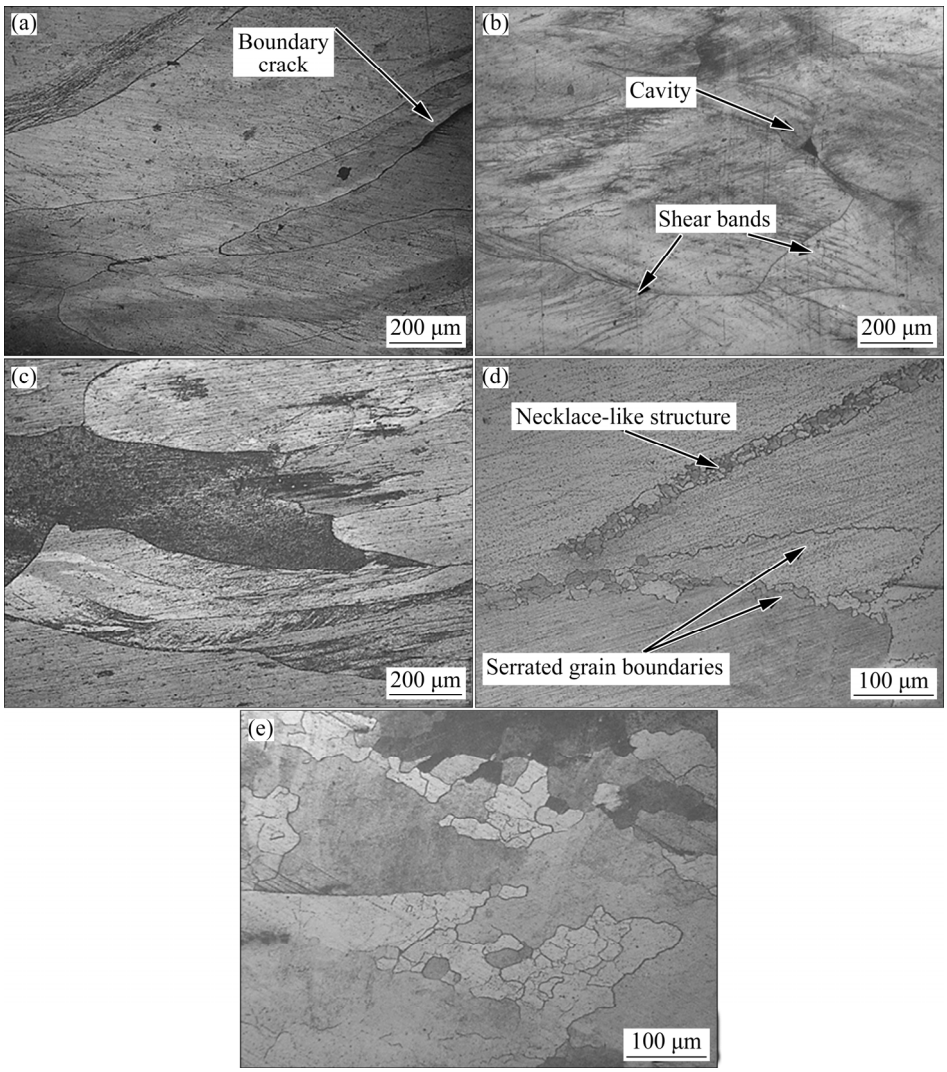

Fig. 3 Microstructures of Cu−3Ti−0.1Zr alloy deformed at different temperatures and strain rates: (a) 700 °C, 1 s^{-1}; (b) 750 °C, 1 s^{-1}; (c) 800 °C, 1 s^{-1}; (d) 750 °C, 0.001 s^{-1}; (e) 850 °C, 0.001 s^{-1}

binding force. Shear bands can also be found in grains. Similar deformation structures are observed in specimen deformed at 800 °C and 1 s^{-1} (Fig. 3(c)). However, deformation structures begin to disappear when the specimens are deformed at a strain rate of 0.001 s^{-1}. Necklace-like structure composed of fine recrystallized grains forms along the original grain boundaries during deformation at 750 °C and 0.001 s^{-1} (Fig. 3(d)). The serrated grain boundaries marked by arrows indicate that DRX occurs. With increasing the deformation temperature to 850 °C (Fig. 3(e)), recrystallized grains coarsen and the distribution of grain sizes becomes inhomogeneous.

3.3 TEM characterization

Figure 4 shows TEM images of dislocations and DRX grains during deformation process. When the alloy is deformed at 700 °C with the strain rate of 1 s^{-1}, the dislocation tangle and cellular structures can be seen in the specimen (Fig. 4(a)), indicating that the density of dislocations in the specimen is quite high. No DRX grains are found in the specimen, suggesting that the dynamic recovery is the main softening mechanism during deformation at low temperature and high strain rate. Density of dislocations is lower as the alloy is deformed at 750 °C and 0.001 s^{-1} in Figs. 4(b, c) than that in Fig. 4(a). Dislocation wall and dislocation network can be observed in Figs. 4(b, c), as well as dislocation pairs. The diffraction spot split in Fig. 4(b) illustrates that lattice distortion occurs. Fine nanoscale DRX grains appear when the specimen is deformed at 800 °C and 1 s^{-1}

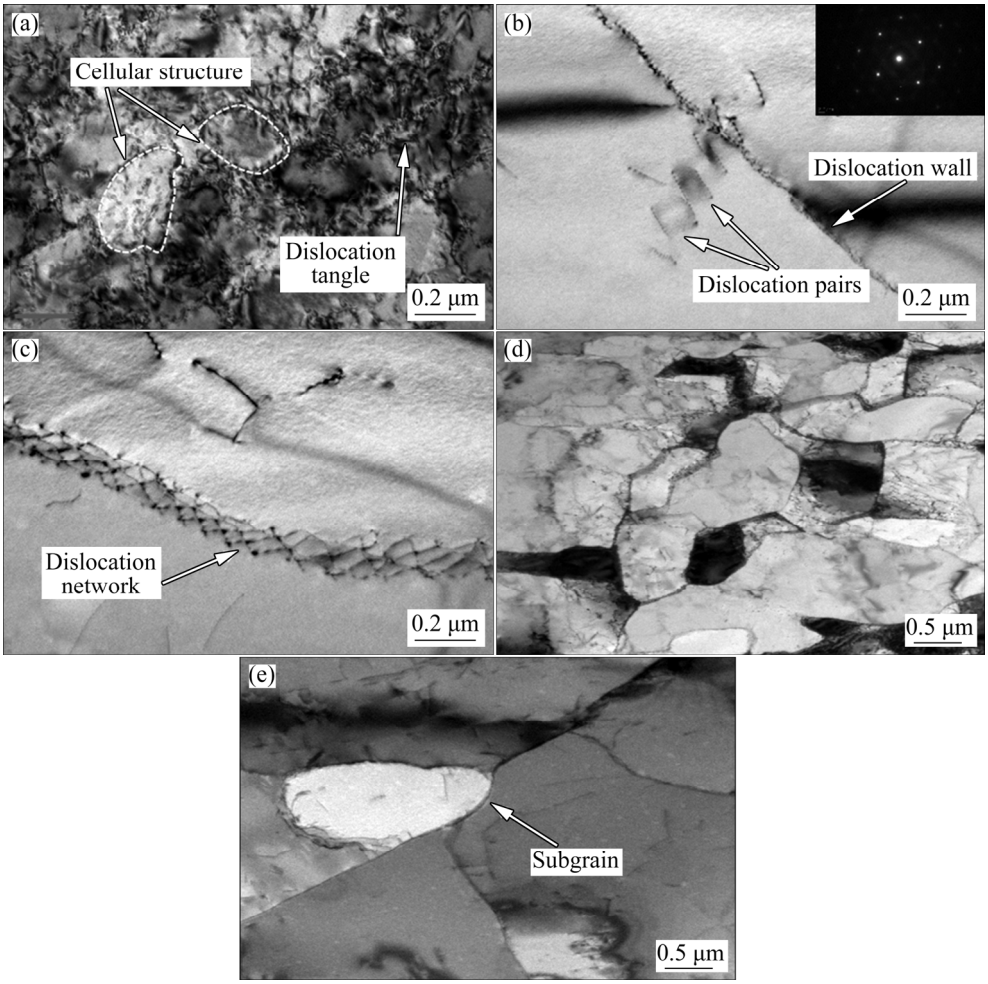

Fig. 4 TEM images of Cu−3Ti−0.1Zr alloy deformed under various conditions: (a) 700 °C, 1 s^{-1}; (b, c) 750 °C, 0.001 s^{-1}; (d) 800 °C, 1 s^{-1}; (e) 800 °C, 0.01 s^{-1}

(Fig. 4(d)). When the strain rate decreases to 0.01 s^{-1}, the recrystallized grains coarsen and subgrains form in recrystallized grains (Fig. 4(e)).

3.4 Construction and verification of constitutive equation

Constitutive equations are widely used to analyze the relationship among the flow stress, strain rate and deformation temperature during the hot deformation process, which can be expressed by the following equations [21]:

$$\dot{\varepsilon} = A_1\sigma^n \exp(-\frac{Q}{RT}), \quad \alpha\sigma<0.8 \tag{1}$$

$$\dot{\varepsilon} = A_2 \exp(\beta\sigma)\exp(-\frac{Q}{RT}), \quad \alpha\sigma>0.8 \tag{2}$$

$$\dot{\varepsilon} = A_3[\sinh(\alpha\sigma)]^m \exp(-\frac{Q}{RT}) \tag{3}$$

$$Z = A_3[\sinh(\alpha\sigma)]^m = \dot{\varepsilon}\exp(\frac{Q}{RT}) \tag{4}$$

where $\dot{\varepsilon}$ is the strain rate (s^{-1}); σ is the flow stress (MPa); Q is the apparent activation energy (kJ/mol) for hot compression deformation; R is the gas constant (8.314 $kJ\cdot mol^{-1}\cdot K^{-1}$); T is the absolute temperature (K); A_1, A_2, A_3, n, β, m and α are material constants ($\alpha=\beta/n$) [22]; Z describes the relationship among flow stress, deformation temperature and strain rate, which called Zener−Hollomon parameter [23,24]. Equations (1) and (2) are applied for the low stress level and high stress level, respectively, while Eq. (3) is suitable for all stress levels. Taking the logarithms of both sides of Eqs. (1), (2), (3) and (4) yields:

$$\ln\dot{\varepsilon} = n\ln\sigma - \frac{Q}{RT} + \ln A_1 \tag{5}$$

$$\ln\dot{\varepsilon} = \beta\sigma - \frac{Q}{RT} + \ln A_2 \tag{6}$$

$$\ln\dot{\varepsilon} = m\ln[\sinh(\alpha\sigma)] - \frac{Q}{RT} + \ln A_3 \tag{7}$$

$$\ln Z = m\ln[\sinh(\alpha\sigma)] + \ln A_3 \quad (8)$$

Figure 5 shows the relations between strain rate and flow stress. According to Eqs. (5) and (6), the value of n is the slope of the linear fits of $\ln\dot{\varepsilon}$ and $\ln\sigma$ in Fig. 5(a) and the value of β is obtained from the slope of linear fits of $\ln\dot{\varepsilon}$ and σ in Fig. 5(b). The average values of n and β are 6.29 and 0.057 MPa^{-1}, respectively. So, α is calculated to be 0.0091 MPa^{-1}.

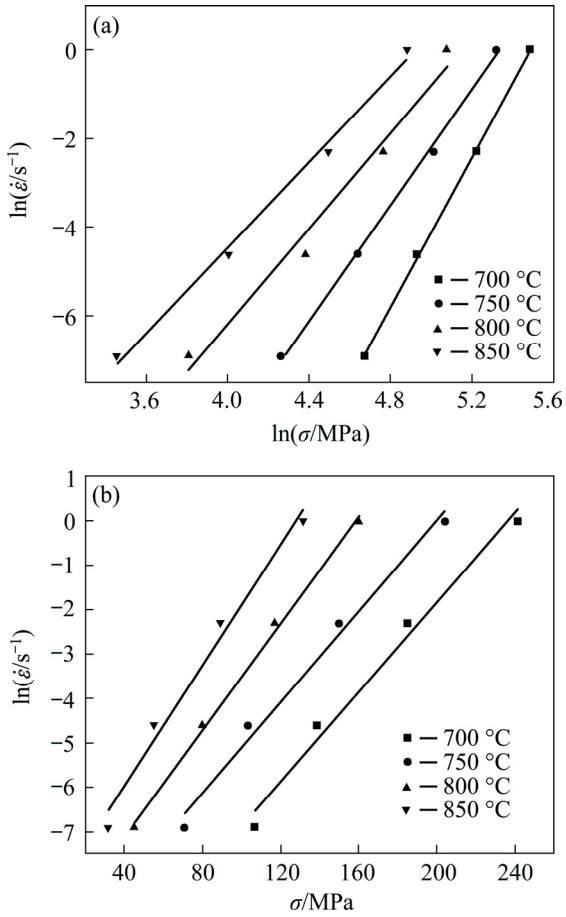

Fig. 5 Relations between strain rate and flow stress: (a) $\ln\dot{\varepsilon}-\ln\sigma$; (b) $\ln\dot{\varepsilon}-\sigma$

Q can be calculated by partial differentiation of Eq. (7), which is expressed as

$$Q = 1000R\left\{\frac{\partial\ln\dot{\varepsilon}}{\partial\ln[\sinh(\alpha\sigma)]}\right\}_T\left\{\frac{\partial\ln[\sinh(\alpha\sigma)]}{\partial(1000/T)}\right\}_{\dot{\varepsilon}} = 1000Rms \quad (9)$$

The linear fits of $\ln\dot{\varepsilon}$ versus $\ln[\sinh(\alpha\sigma)]$ at different temperatures and $\ln[\sinh(\alpha\sigma)]$ versus T^{-1} at various strain rates are shown in Figs. 6(a) and (b). m and s are the average slopes of the plotted lines with the values of 4.54 and 8.46, respectively. Therefore, the apparent activation energy Q for the designed alloy is calculated to be 319.56 kJ/mol. Figure 6(c) displays the plotted line of $\ln Z$ versus $\ln[\sinh(\alpha\sigma)]$ and $\ln A_3$ is the intercept which is calculated to be 32.5.

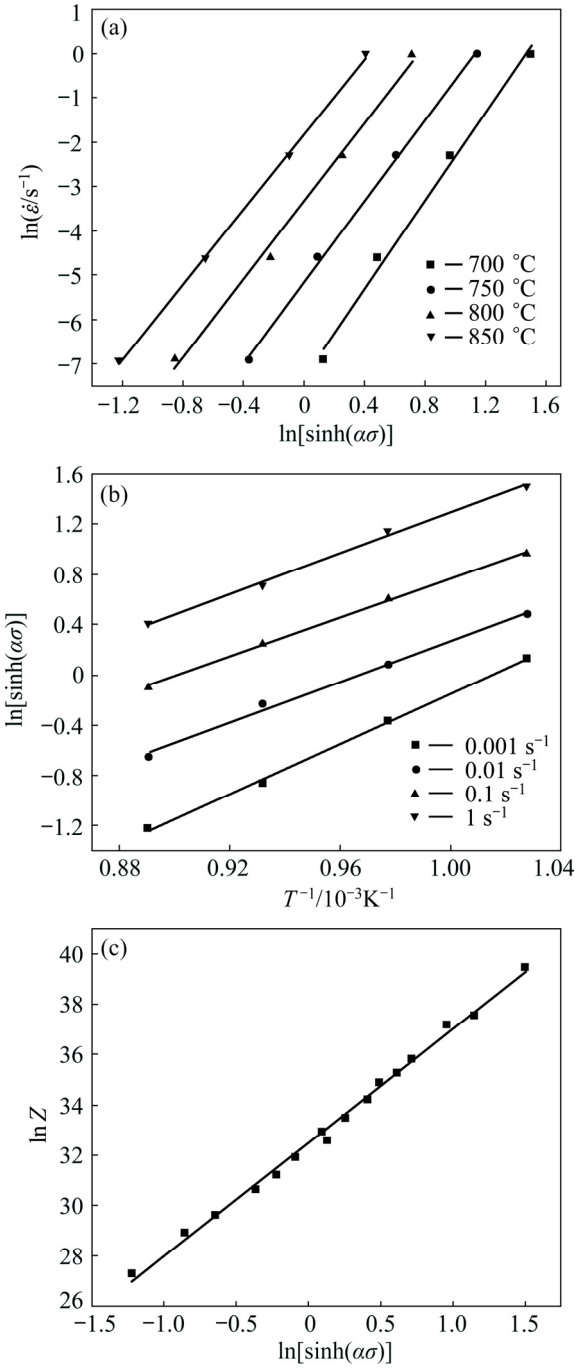

Fig. 6 Relations of $\ln\dot{\varepsilon}$ vs $\ln[\sinh(\alpha\sigma)]$ (a), $\ln[\sinh(\alpha\sigma)]$ vs T^{-1} (b), and $\ln Z$ vs $\ln[\sinh(\alpha\sigma)]$ (c)

On the basis of above analysis, the constitutive equation of Cu−3Ti−0.1Zr alloy can be expressed as

$$\dot{\varepsilon} = e^{32.5}[\sinh(0.0091\sigma)]^{4.54}\exp[-319.56/(RT)] \quad (10)$$

It is necessary to point out that the stress (σ)

used in the above calculation is that at the true strain of 0.8. Since material constants are related with strain [25], the effect of strain on constitutive equations can not be ignored. In order to study the change of material constants under different deformation degrees, different stress values at the true strains from 0.1 to 0.8 at an interval of 0.05 are used. The curves of α, m, Q and $\ln A_3$ are shown in Fig. 7. They are expressed in the form of Eq. (11) with 6-order polynomials:

$$\alpha(\varepsilon)=B_0+B_1\varepsilon+B_2\varepsilon^2+B_3\varepsilon^3+B_4\varepsilon^4+B_5\varepsilon^5+B_6\varepsilon^6$$

$$m(\varepsilon)=C_0+C_1\varepsilon+C_2\varepsilon^2+C_3\varepsilon^3+C_4\varepsilon^4+C_5\varepsilon^5+C_6\varepsilon^6$$

$$Q(\varepsilon)=D_0+D_1\varepsilon+D_2\varepsilon^2+D_3\varepsilon^3+D_4\varepsilon^4+D_5\varepsilon^5+D_6\varepsilon^6$$

$$\ln A_3(\varepsilon)=E_0+E_1\varepsilon+E_2\varepsilon^2+E_3\varepsilon^3+E_4\varepsilon^4+E_5\varepsilon^5+E_6\varepsilon^6 \quad (11)$$

Table 1 lists the results of the polynomial fitting. According to Eq. (11) and results in Table 1, parameters α, m, Q and $\ln A_3$ under various strains are calculated. Equation (7) can also be written as

$$\sigma=\frac{1}{\alpha}\sinh^{-1}\left[\frac{\dot{\varepsilon}\exp[Q/(RT)]}{A_3}\right]^{\frac{1}{m}} \quad (12)$$

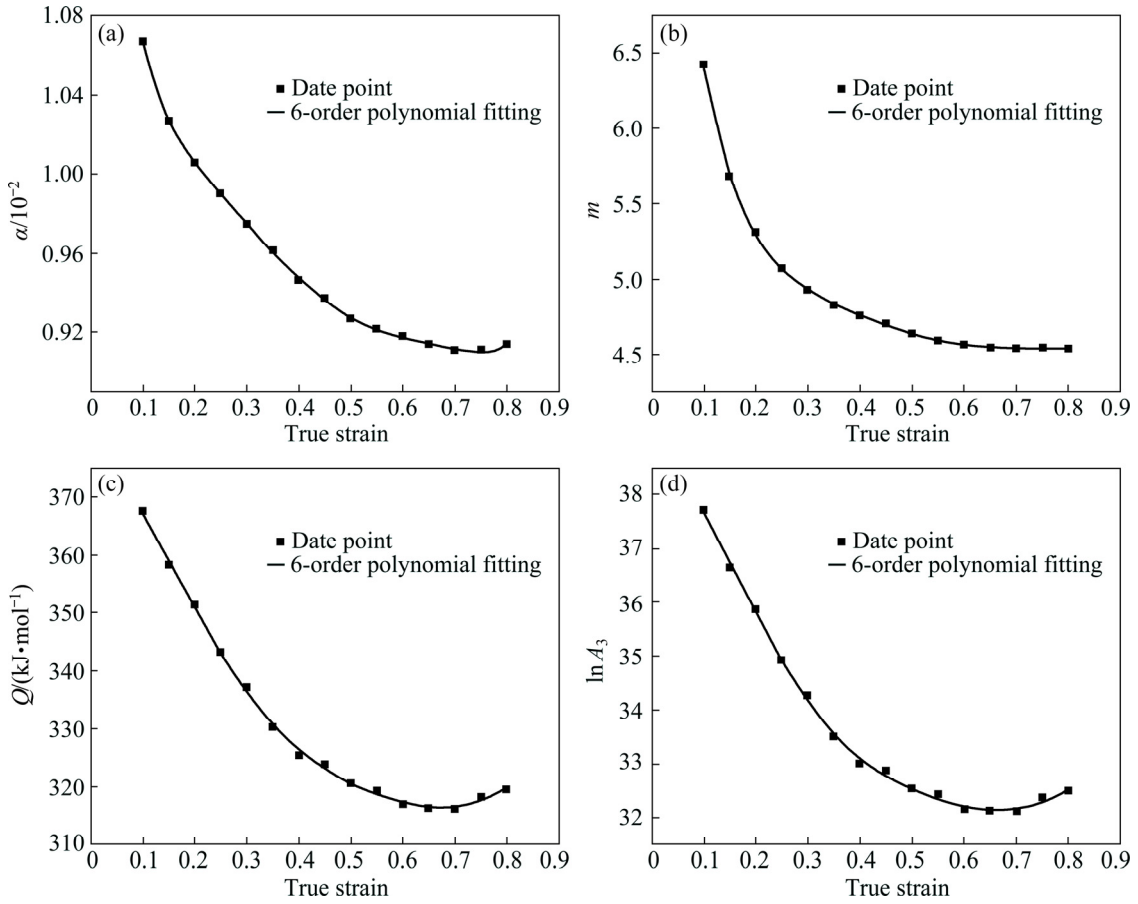

Fig. 7 6-order polynomials curves of α (a), m (b), Q (c) and $\ln A_3$ (d)

Table 1 Coefficient of polynomial fitting for material constants

α	m	Q	$\ln A_3$
B_0=0.01284	C_0=9.72196	D_0=3.78×10^5	E_0=38.59017
B_1=−0.03772	C_1=−51.79347	D_1=−27123.52	E_1=3.76493
B_2=0.21992	C_2=240.76911	D_2=−1.10×10^6	E_2=−184.21944
B_3=−0.71168	C_3=−609.61086	D_3=3.75×10^6	E_3=657.96603
B_4=1.2354	C_4=853.79375	D_4=−5.36×10^6	E_4=−1052.4504
B_5=−1.0825	C_5=−620.81114	D_5=3.54×10^6	E_5=814.02525
B_6=0.37691	C_6=183.09877	D_6=−8.26×10^5	E_6=−243.0147

With Eq. (12) and calculated parameters, the flow stress of Cu−3Ti−0.1Zr alloy under different deformation conditions can be achieved. The predicted values from flow stress model and experimental value from compression testing are shown together in Fig. 8. It can be seen that in most conditions, calculated values and experimental values are consistent with each other.

3.5 Hot processing map

Hot processing maps based on dynamic material model (DMM) have been widely used to guide hot deformation processes. DMM given by Prasad is built on continuum mechanics and irreversible thermodynamics [26]. According to this model, the workpiece is considered to be an energy dissipater during the deformation process. The total power dissipation (P) includes two parts: the plastic deformation relevant to the heat dissipation effects (G) and the metallurgical microstructures evolution relevant to the power dissipation (J). The total power dissipation can be described as follows:

$$P=\sigma\dot{\varepsilon}=G+J=\int_0^{\dot{\varepsilon}}\sigma \mathrm{d}\dot{\varepsilon}+\int_0^{\sigma}\dot{\varepsilon}\mathrm{d}\sigma \tag{13}$$

The proportion of G and J is determined by a strain rate sensitivity of the flow stress (m'), which can be expressed as [27]

$$m'=\frac{\mathrm{d}J}{\mathrm{d}G}=[\frac{\partial(\ln\sigma)}{\partial(\ln\dot{\varepsilon})}]_{\varepsilon,T} \tag{14}$$

At a given temperature, $\dot{\varepsilon}$, σ and m' conform to dynamic constitutive equation:

$$\sigma=k\dot{\varepsilon}^{m'} \tag{15}$$

Therefore, J can be re-written as

$$J=\int_0^{\sigma}\dot{\varepsilon}\mathrm{d}\sigma=\frac{m'\sigma\dot{\varepsilon}}{m'+1} \tag{16}$$

For ideal linear dissipation, m'=1 and $J=J_{max}=\sigma\dot{\varepsilon}/2=P/2$. For nonlinear dissipation, parameter η is used to evaluate the efficiency of power dissipation during hot deformation:

$$\eta=\frac{J}{J_{max}}=\frac{2m'}{m'+1} \tag{17}$$

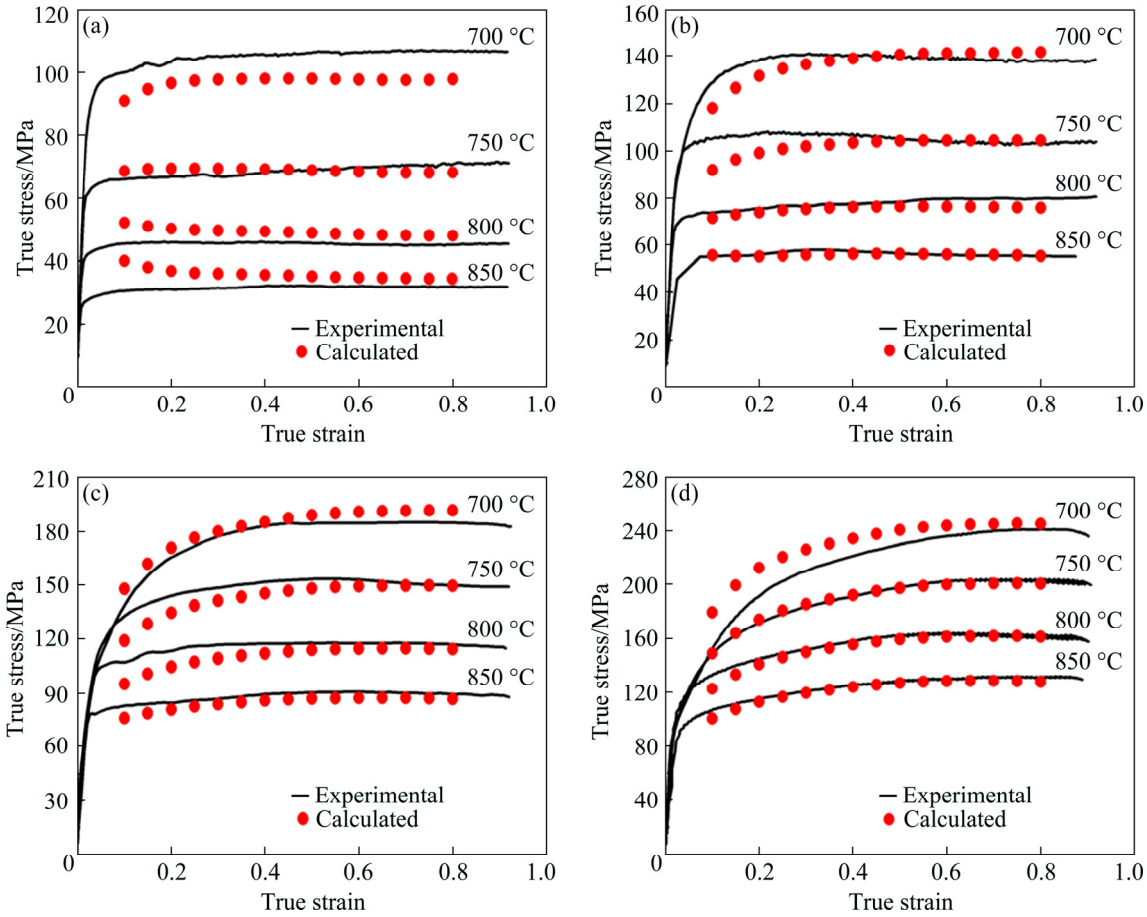

Fig. 8 Comparison of experimental value and calculated value of flow stress under different conditions: (a) 0.001 s^{-1}; (b) 0.01 s^{-1}; (c) 0.1 s^{-1}; (d) 1 s^{-1}

The power dissipation map contains all the value of η calculated at various deformation temperatures and strain rates. The instability map is developed based on the extremum principles of irreversible thermodynamics. The flow instabilities parameter $\xi(\dot{\varepsilon})$ can be defined as [28]

$$\xi(\dot{\varepsilon})=\frac{\partial \ln[m'/(m'+1)]}{\partial \ln \dot{\varepsilon}}+m'\leq 0 \tag{18}$$

The instability map includes all the values of $\xi(\dot{\varepsilon})$ at different temperatures and strain rates. When $\xi(\dot{\varepsilon})$ is negative, flow instabilities could occur. Then, $\lg\sigma$ can be expressed with $\lg\dot{\varepsilon}$ as

$$\lg\sigma=a+b\lg\dot{\varepsilon}+c(\lg\dot{\varepsilon})^2+d(\lg\dot{\varepsilon})^3 \tag{19}$$

Therefore, the following equations are achieved:

$$m'=\frac{\mathrm{d}(\lg\sigma)}{\mathrm{d}(\lg\dot{\varepsilon})}=b+2c\lg\dot{\varepsilon}+3d(\lg\dot{\varepsilon})^2 \tag{20}$$

$$\xi(\dot{\varepsilon})=\frac{2c+6d\lg\dot{\varepsilon}}{m'(m'+1)\ln 10}+m' \tag{21}$$

First, the parameters of power dissipation and instabilities in the experimental deformation conditions are calculated, and then inner mesh interpolation method is used to supplement the values of power dissipation and instabilities under the nonexperimental deformation conditions. Using Eq. (17) and Eq. (21), the hot processing map of Cu−3Ti−0.1Zr alloy deformed at the strain of 0.6 and 0.9 are shown in Figs. 9(a) and (b), respectively. Shaded domains represent unstable regions and the contour lines represent the efficiency of power dissipation η. It can be seen that the value of efficiency of power dissipation is high at high deformation temperature and low strain rate regions. According to Fig. 9(a), the peak efficiency is about 45% in the temperature range of 775−825 °C with the strain rate around 0.001 s^{-1} (Domain C). Domain A occurs at low temperature from about 700 to 750 °C with high strain rate over 0.1 s^{-1}, where efficiency of power dissipation is low at the same time. It is often considered as the instability region. Domain B is another instability region which happens at about 850 °C with strain rate over 0.1 s^{-1}. When specimens are deformed in Domains A and B, flow instabilities can take place. At the true strain of 0.9, Domain D in the temperature range of 700−750 °C with low strain rate is instability region as well as low efficiency of power dissipation region. In Domain E at approximately 800 °C, the highest η is 47%.

Domains C and E with the highest η are away from unstable regions, so specimens deformed in Domains C and E have good workability. According to the hot processing maps in Fig. 9, the optimized parameters for the hot deformation of Cu−3Ti−0.1Zr alloy is 775−850 °C with the strain rate between 0.001 and 0.01 s^{-1}.

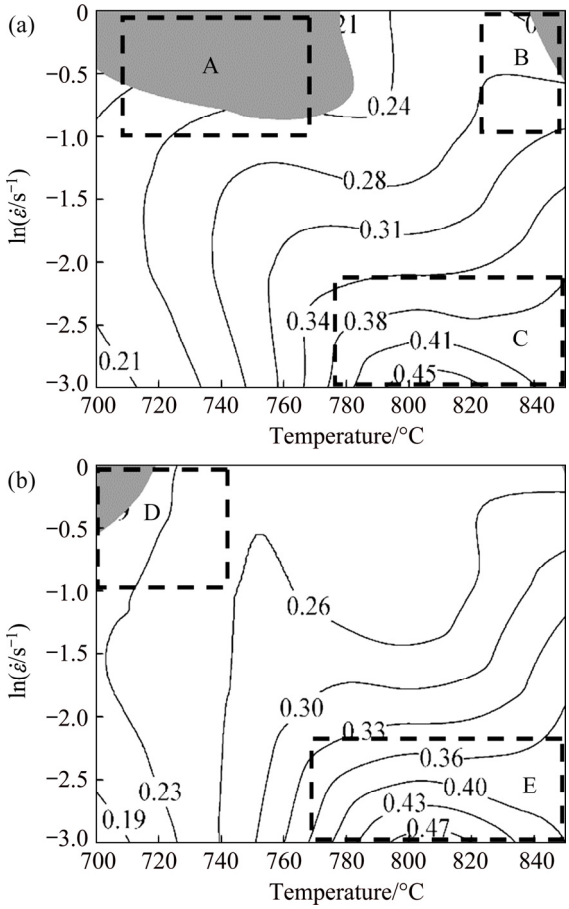

Fig. 9 Hot processing maps of Cu−3Ti−0.1Zr alloy at different true strains: (a) 0.6; (b) 0.9

3.6 Discussion

At the early stage of the compression, dislocation density increases rapidly and then work hardening causes the sharp rise of flow stress [14]. At the same time, deformation energy increases and stores in the severe deformation zone, which will promote dynamic recrystallization later [29,30]. According to the flow stress curves (Fig. 2), dynamic recrystallization is easy to occur at low strain rate or high temperature in hot deformed alloys, as they provide enough time for energy accumulation and thermal activation energy for DRX. DRX grains preferentially nucleate along

original grain boundaries because of the high distortion energy on boundaries [31].

In Fig. 3(d), serrated boundaries result from bulging of original boundaries due to local migration. The strain-induced local grain boundary migration can sweep away dislocations. Necklace-like recrystallization grains misaligned with original grains form finally. The emergence of necklace structure indicates that the dominant dynamic recrystallization nucleation mechanism is grain boundary migration [32].

The accuracy of the established constitutive equation can be seen from the comparison between the experimental values and calculated values of flow stress, as shown in Fig. 8. The experimental values and calculated values are accordant with each other under most deformation conditions. However, the error between the two values is a little large at the small true strain. The phenomenon is probably caused by the simplification treatment. When the samples are compressed at the low true strain, the deformation process is not easy to reach steady state and plastic deformation stage completely. In the constitutive equations, the parameters including n, β, m and α are assumed to be constants that are unrelated with the deformation temperature or strain rate. However, the slopes in Fig. 5 and Fig. 6 which represent the parameters are different and the average values are taken, leading to a relative large error between the experimental values and calculated values at the low true strain.

In the hot processing maps, there are stability deformation domains as well as instability deformation domains. The former ones usually result from dynamic recovery and dynamic recrystallization. Instability domains are associated with shear bands, flow localization, adiabatic deformation bands, flow rotations and mechanical twinning [33,34]. In Domain D which represents high strain rate and low deformation temperature, a large amount of dislocations are found (Fig. 4(a)) and the lattice distortion happens at the interface, leading to the stress concentration [35]. When the stress concentration exceeds the alloy strength, cracks form along the grain boundaries as Fig. 3(a) shows.

4 Conclusions

(1) The flow stress of Cu−3Ti−0.1Zr alloy increases with decreasing deformation temperature and increasing strain rate. The flow characteristics of Cu−3Ti−0.1Zr alloy deformed at a true strain of 0.8 can be expressed in the form of constitutive equation:

$$\dot{\varepsilon} = \mathrm{e}^{32.5}[\sinh(0.0091\sigma)]^{4.54} \exp(-319.56/(RT))$$

The apparent activation energy Q is calculated to be 319.56 kJ/mol. The constitutive equation can predict the flow stress of the alloy during hot compression well.

(2) Hot processing maps are established which show that the appropriate condition for hot compression is from 775 to 850 °C with a strain rate from 0.001 to 0.01 s^{-1}. When the samples are deformed at true strain of 0.9, the flow instability zone appears at the deformation temperature of 700−725 °C with strain rate of 1 s^{-1}.

(3) Subgrains and DRX grains tend to appear in specimens deformed at high temperatures or low strain rates.

References

[1] XIAO Xiang-peng, YI Zhi-yong, CHEN Ting-ting, LIU Rui-qing, WANG Hang. Suppressing spinodal decomposition by adding Co into Cu−Ni−Si alloy [J]. Journal of Alloys and Compounds, 2016, 660: 178−183.

[2] ZHOU Yan-jun, SONG Ke-xing, XING Jian-dong, ZHANG Yan-min. Precipitation behavior and properties of aged Cu−0.23Be−0.84Co alloy [J]. Journal of Alloys and Compounds, 2016, 658: 920−930.

[3] LEI Qian, LI Zhou, WANG Ming-pu, ZHANG Liang, GONG Shen, XIAO Zhu. Phase transformations behavior in a Cu−8.0Ni−1.8Si alloy [J]. Journal of Alloys and Compounds, 2011, 509: 3617−3622.

[4] JEON W S, SHUR C C, KIM J G, HAN S Z, KIM Y S. Effect of Cr on the corrosion resistance of Cu−6Ni−4Sn alloys [J]. Journal of Alloys and Compounds, 2008, 455: 358−363.

[5] ZHANG Hong-tao, JIANG Yan-bing, XIE Jian-xin, LI Yong-hua, YUE Li-juan. Precipitation behavior, microstructure and properties of aged Cu−1.7 wt% Be alloy [J]. Journal of Alloys and Compounds, 2019, 773: 1121−1130.

[6] SOFFA W A, LAUGHLIN D E. High-strength age hardening copper−titanium alloys: Redivivus [J]. Progress in Materials Science, 2004, 49: 347−366.

[7] YI Jiang, JIA Yan-lin, ZHAO Yu-yuan, XIAO Zhu, HE Ke-jian, WANG Qi, WANG Ming-pu, LI Zhou. Precipitation behavior of Cu−3.0Ni−0.72Si alloy [J]. Acta Materialia, 2019, 166: 261−270.

[8] JIANG Ye-xin, LI Zhou, XIAO Zhu, XING Yan. ZHANG Yang, FANG Mei. Microstructure and properties of a Cu−Ni−Sn alloy treated by two-stage thermomechanical processing [J]. JOM, 2019, 71: 2734−2741.

[9] CAO Xing-min, ZHU Yu-bin, GUO Fu-an, TANG Yu-qiong, XIANG Chao-jian, YANG Chun-xiu. Hot deformation behavior and microstructure of Cu−Ti Alloy [J]. Rare Metal Materials and Engineering, 2009, 38: 509−514. (in Chinese)

[10] YANG Qing-bo, DENG Yan-jun, YANG Mou, ZHANG Zhi-qing, LI Wei-guo, LIU Qing. Effect of Al_3Zr particles on hot-compression behavior and processing map for Al−Cu−Li based alloys at elevated temperatures [J]. Transactions of Nonferrous Metals Society of China, 2020, 30: 872−882.

[11] XIA Yu-feng, JIANG Wei, CHENG Qian, JIANG Lai, JIN Li. Hot deformation behavior of Ti−6Al−4V−0.1Ru alloy during isothermal compression [J]. Transactions of Nonferrous Metals Society of China, 2020, 30: 134−146.

[12] ZHONG Li-ping, WANG Yong-jian. Microstructure evolution and optimum parameters analysis for hot working of new type Mg−8Sn−2Zn−0.5Cu alloy [J]. Transactions of Nonferrous Metals Society of China, 2019, 29: 2290−2299.

[13] ZHAO Chao, WANG Zhi, PAN De-qing, LI Dao-xi, LUO Zong-qiang, ZHANG Da-tong, YANG Chao, ZHANG Wei-wen. Effect of Si and Ti on dynamic recrystallization of high-performance Cu−15Ni−8Sn alloy during hot deformation [J]. Transactions of Nonferrous Metals Society of China, 2019, 29: 2556−2565.

[14] LIU Jia, WANG Xian-hui, LIU Ji-tuo, LIU Yan-feng, LI Hang-yu, WANG Chan. Hot deformation and dynamic recrystallization behavior of Cu−3Ti−3Ni−0.5Si alloy [J]. Journal of Alloys and Compounds, 2019, 782: 224−234.

[15] BAHU K A, MANDAL S, ATHREYA C N, SHAKTHIPRIYA B, SARMA V S. Hot deformation characteristics and processing map of a phosphorous modified super austenitic stainless steel [J]. Materials and Design, 2017, 115: 262−275.

[16] HUMPHREYS F J, KALU P N. Dislocation−particle interactions during high temperature deformation of two-phase aluminium alloys [J]. Acta Metallurgica, 1987, 35: 2815−2829.

[17] YAN Jie, PAN Qing-lin, ZHANG Xiang-kai, SUN Xue, LI An-de, ZHOU Xun. Characterization of hot deformation behavior of Al−Zn−Mg−Mn−Zr alloy during compression at elevated temperature [J]. Journal of Central South University, 2017, 24: 515−520.

[18] GAPONOVA O P, BAGLYUK G A. Effect of temperature–rate strain conditions on the power variables and structurization during hot-forging of the sintered Cu−2%Ti billets [J]. Powder Metallurgy and Metal Ceramics, 2016, 55: 406−412.

[19] SZKLINIARZ A, SZKLINIARZ Z, BLACHA L. Microstructure of hot-deformed Cu−3Ti alloy [J]. Archives of Metallurgy and Materials, 2016, 61: 347−352.

[20] LI Chen-wei, XIE Hui, MAO Xiao-nan, ZHANG Peng-sheng, HOU Zhi-ming. High temperature deformation of TC18 titanium alloy [J]. Rare Metal Materials and Engineering, 2017, 46: 326−332.

[21] MIRZADEH H, CABRERA J M, NAJAFIZADEH A. Constitutive relationships for hot deformation of austenite [J]. Acta Materialia, 2011, 59: 6441−6448.

[22] McQUEEN H J, RYAN N D. Constitutive analysis in hot working [J]. Materials Science and Engineering A, 2002, 322: 43−63.

[23] ZENER C, HOLLOMON J H. Effect of strain rate upon plastic flow of steel [J]. Journal of Applied Physics, 1944, 15: 22−32.

[24] SLOOFF F A, ZHOU J, DUSZCZYK J, KATGERMAN L. Constitutive analysis of wrought magnesium alloy Mg−Al4−Zn1 [J]. Scripta Materialia, 2007, 57: 759−762.

[25] LIN Yong-cheng, WEN Dong-xu, DENG Jiao, LIU Guan, CHEN Jian. Constitutive models for high-temperature flow behaviors of a Ni-based superalloy [J]. Materials and Design, 2014, 59: 115−123.

[26] PRASAD Y V R K, GEGEL S M D H L, MALAS J C, MORGAN J T, LARK K A, BARKER D R. Modeling of dynamic material behavior in hot deformation: Forging of Ti-6242 [J]. Metallurgical Transactions A, 1984, 15: 1883−1892.

[27] PRASAD Y V R K, RAO K P. Processing maps and rate controlling mechanisms of hot deformation of electrolytic tough pitch copper in the temperature range 300−950 °C [J]. Materials Science and Engineering A, 2005, 391: 141−150.

[28] LIN Yong-cheng, LI Lei-ting, FU Yan-xiang, JIANG Yu-qiang. Hot compressive deformation behavior of 7075 Al alloy under elevated temperature [J]. Journal of Materials Science, 2011, 47: 1306−1318.

[29] MIRZADEH H, PARSA M H. Hot deformation and dynamic recrystallization of NiTi intermetallic compound [J]. Journal of Alloys and Compounds, 2014, 64: 56−59.

[30] LEI Qian, LI Zhou, ZHU An-yin, QIU Wen-ting, LIANG Shu-quan. The transformation behavior of Cu−8.0Ni−1.8Si−0.6Sn−0.15Mg alloy during isothermal heat treatment [J]. Materials Characterization, 2011, 62: 904−911.

[31] QUAN Guo-zheng, LI Gui-sheng, CHEN Tao, WANG Yi-xin, ZHANG Yan-wei, ZHOU Jie. Dynamic recrystallization kinetics of 42CrMo steel during compression at different temperatures and strain rates [J]. Materials Science and Engineering A, 2011, 528: 4643−4651.

[32] MOMENI A, ABBASI S M, MORAKABATI M, BADRI H, WANG X. Dynamic recrystallization behavior and constitutive analysis of Incoloy 901 under hot working condition [J]. Materials Science and Engineering A, 2014, 615: 51−60.

[33] WANG Bing-jie, ZHANG Yi, TIAN Bao-hong, AN Jun-chao, VOLINSKY A A, SUN Hui-li, LIU Yong, SONG Ke-xing. Effects of Ce addition on the Cu−Mg−Fe alloy hot deformation behavior [J]. Vacuum, 2018, 155: 594−603.

[34] ZHANG Yi, LIU Ping, TIAN Bao-hong, LIU Yong, LI Rui-qin, XU Qian-qian. Hot deformation behavior and processing map of Cu−Ni−Si−P alloy [J]. Transactions of Nonferrous Metals Society of China, 2013, 23: 2341−2347.

[35] ZHANG Yi, CHAI Zhe, VOLINSKY A A, SUN Hui-li, TIAN Bao-hong, LIU Ping, LIU Yong. Hot deformation characteristics and processing maps of the Cu−Cr−Zr−Ag alloy [J]. Journal of Materials Engineering and Performance, 2016, 25: 1191−1198.

超高强 Cu−3Ti−0.1Zr 合金的显微组织演变和热变形行为

王 旭[1]，李 周[1,2]，肖 柱[1,3]，邱文婷[1]

1. 中南大学 材料科学与工程学院，长沙 410083；
2. 中南大学 粉末冶金国家重点实验室，长沙 410083；
3. 有色金属材料科学与工程教育部重点实验室，长沙 410083

摘 要：采用 Gleeble−3500 热模拟器在不同温度(700~850 °C)和不同应变速率(0.001~1 s^{-1})下，对超高强导电 Cu−3Ti−0.1Zr 合金的热压缩变形行为进行研究。结果表明，合金在热变形过程中发生加工硬化、动态回复以及动态再结晶。建立合金在真应变为 0.8 情况下的热压缩本构方程，并且得到在此情况下热变形激活能 Q 为 319.56 kJ/mol。在不同应变下，流变应力的实验值和计算值之间的误差很小，说明建立的本构方程可以很好地描述 Cu−3Ti−0.1Zr 合金的热变形行为。以动态材料模型为基础建立合金的热加工图，从图中可知合金的理想热加工温度范围为 775~850 °C, 应变速率范围为 0.001~0.01 s^{-1}。

关键词：Cu−3Ti−0.1Zr 合金；热变形；本构方程；再结晶；热加工图

(Edited by Bing YANG)